Numerical Analysis of Thermal and Electrochemical Phenomena for Anode Supported Microtubular SOFC

Daan Cui
Dalian National Laboratory for Clean Energy, Dalian 116023, P.R. China

Dalian Institute of Chemical Physics, Chinese Academy of Sciences, 457 Zhongshan Road, Dalian 116023, P.R. China.

Graduate School of the Chinese Academy of Sciences, Beijing 100049, P.R. China

Mojie Cheng
Dalian National Laboratory for Clean Energy, Dalian 116023, P.R. China

Dalian Institute of Chemical Physics, Chinese Academy of Sciences, 457 Zhongshan Road, Dalian 116023, P.R. China

DOI 10.1002/aic.11697
Published online January 22, 2009 in Wiley InterScience (www.interscience.wiley.com).

A 2D model considering momentum, heat/species transport and electrochemical phenomena, has been proposed for tubular solid oxide fuel cell. The model was validated using experimental polarization curves and the good agreement with the experimental data was attained. The temperature distributions show that temperature varies severely at the tube inlet than at the tube outlet. The heat generation and transfer mechanisms in electrodes, electrolyte and electrochemical reaction interface were investigated. The results show that the overall electrochemical reaction heat is produced at cathode/electrolyte interface, and a small portion of the heat is consumed at anode/electrolyte interface. The heat produced at cathode/electrolyte interface is about five times as much as that consumed at anode/electrolyte interface. Overwhelming part of the heat transfer between cell and outside occurs at cathode external surface. Most current flow goes into anode from a very small area where the current collectors locates. © 2009 American Institute of Chemical Engineers *AIChE J,* 55: 771–782, 2009
Keywords: solid oxide fuel cells, microtube, modeling, current collection, heat transfer

Introduction

Solid oxide fuel cells (SOFCs) are promising candidates for power generation technology because of their high efficiency, silent work and clean generation of electric power.[1,2] The main concerns in the road to commercialization are cost, performance and reliability. Several different cell designs are being investigated.[1] Thermal management in SOFCs is an important issue because the extremely high local temperature can lead to mechanical failures even under steady-state operations, which can be investigated with a mathematical model.[1,3]

Most thermal and electrochemical model have been proposed for the cathode-supported tubular and anode-supported

Correspondence concerning this article should be addressed to M. J. Cheng at mjcheng@dicp.ac.cn.

Table 1. Input Parameters to Model[2,8,14,15]

Descriptions	Symbol	Value
Furnace interior diameter (mm)		6
Tubular interior diameter (mm)		1.49
Anode thickness (mm)		0.72
Cathode thickness (μm)		50
Electrolyte thickness (μm)		50
Anode conductivity (S/m)	σ_a	9320exp(303.1/T)*
Cathode conductivity (S/m)	σ_c	$42\times10^6/T\exp(-1200/T)$
Electrolyte conductivity (S/m)	σ_{ele}	$3.34\times10^4\exp(-10300/T)$
Anode thermal conductivity (W/m K)	k_a	1.86
Cathode thermal conductivity (W/m K)	k_{ele}	2.16
Electrolyte thermal conductivity (W/m K)	k_c	5.84
Anode density (kg/m^3)	ρ_a	3310
Electrolyte density (kg/m^3)	ρ_{ele}	5160
Cathode density (kg/m^3)	ρ_c	3030
Anode specific heat capacity [J/(kg·K)]	$C_{P,a}$	450
Electrolyte specific heat capacity [J/(kg·K)]	$C_{P,ele}$	430
Cathode specific heat capacity [J/(kg·K)]	$C_{P,c}$	470
Activation energy of anode (J/mol)	$E_{act,a}$	140,000
Transfer coefficient	β	0.5
Electron transferred per reacting	n_e	1
Permeability (m^2)	K	1×10^{-12}
Molar entropy change of cathode reaction (J/mol K)	ΔS_c	81.63
O_2 Fuller diffusion volume	V_{O_2}	16.3
N_2 Fuller diffusion volume	V_{N_2}	18.5
H_2 Fuller diffusion volume	V_{H_2}	6.12
H_2O Fuller diffusion volume	V_{H_2O}	13.1
Porosity	ε	30%
Tortuosity factor	τ	10
Thermal radiative emissivity	ε_{rad}	0.3
Porous radius (m)	r_p	5×10^{-7}

*Curve fitting according to the experimenal data.

planar SOFCs.[3–8] In 1994, Achenbach[5] has used unit cells and solved the transport equations including the electrochemical reactions though a 3D and time-dependent model for planar SOFC. Achenbach's model is quite accurate, but many physical processes were not explained including momentum transport and the change of partial pressure in the electrodes. Some of these issues are solved in the later models. For example, Yakabe et al.[7,8] performed a 3D model on planar SOFCs, which makes it possible to simulate the current flow in a cell, and the effects of the geometry of the cell components on the cell performance was considered perfectly in the calculation. Sanchez et al.[3] developed a 2D axisymmetric model of a tubular SOFC and analyzed electrochemistry and heat transfer inside the cell, including radiative heat exchange between the anodic gas and the anode surface in order to evaluate its effect on global performance. The current SOFC model is mostly to use computational fluid dynamics to solve the transport equations and couple the solution to an electrochemical model. Recent years, because of more rapid starting and higher volume power density, anode supported microtubular SOFC has been rapidly developed.[2,8–13] Due to much longer current path in this type SOFC, Bove[8] and Cui et al.[2] investigated the effect of different current collecting modes for anode supported microtubular SOFC through mathematical modeling. However, the previous model can not deal with the temperature distribution, which depends on the current density distribution and the heat transfer. In order to investigate the effect of the different current collecting modes on the temperature distribution, it is necessary to develop a new specific model for the investigation of the temperature distribution in the cell components.

The model presented in this article covers momentum, electro-chemical and heat/species transport, and gives a valuable and high efficient method for the analysis of microtubular SOFC. The three current collecting modes proposed previously will be investigated with the detailed thermal and electrochemical model. The temperature distribution in cell, the current density distribution in anode and electrolyte and heat transfer phenomena under the three different current collecting modes are analyzed.

Experimental

Anode electrical conductivity measurements

Electrical conductivity of the porous substrate is one of the key performance-limiting factors for the anode-supported micro tubular SOFCs in this article. Electrical conductivity of the sintered microtubular porous anodic substrate was measured by the four-terminal DC method using a Keithley 2000 Multimeter under the hydrogen atmosphere from 800°C to 300°C. The fitted equation of the measured anodic conductivity (σ_a) was shown at Table 1.

Single cell performance measurements

The anode supported tubular cell consists of YSZ electrolyte, Ni-YSZ anode and LSM-YSZ cathode. The thicknesses of the anode, cathode and electrolyte were 720, 50, and 20 μm, respectively. The internal diameter of the cell is 1.39 mm and cell

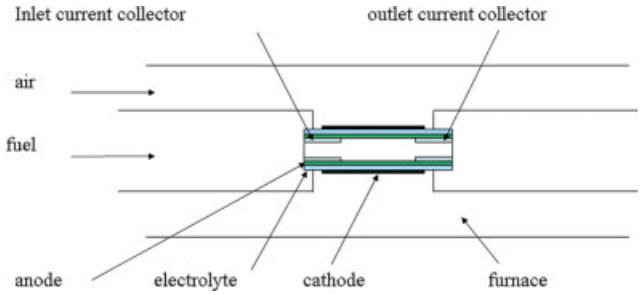

Figure 1. The diagram of the microtubular cell reactor.

[Color figure can be viewed in the online issue, which is available at www.interscience.wiley.com.]

length is 60 mm. Figure 1 shows the diagram of the micro tubular cell reactor. The tubular cell locates in the center of the furnace whose wall temperature is 800°C. The inlet fuel was composed of H_2 and H_2O (0.97:0.03 in molar fractions), flowing at a volume velocity of 30 cm^3/min at room temperature. The fuel gas was preheated to 800°C before entering the cell. Air flow rate at the cathode channel inlet was 60 cm^3/min. The current collector at the anode side was attached to the inner surfaces of both ends of anode tube, whereas the current collector at the cathode side was connected to the whole cathode. The Ag wire with a silver mesh was used for collecting current.

Microtubular SOFC Model

General description

Because the tubular cell has a symmetrical structure, the 2D modeling is considered for the entire cell performance, as shown in Figure 2. The dimensions of the cell are listed in Table 1. From Figures 1 and 2, it can be found that the current collectors locate at two ends of the internal part of anode substrate. IC, OC, and BC express that the current collectors locate at the fuel inlet, fuel outlet and both inlet and outlet, respectively. The following assumptions are used in this model:

- The model is based on steady state, using humidified H_2 as the fuel.
- Gas flow in the electrode channel is a fully developed laminar flow.
- The reactant gas mixtures are approximated as ideal gas and incompressible. The fuel cell operates with 100% current efficiency.
- The electrochemical reactions are considered to only take place at the electrode/electrolyte interface.
- The model neglects any interaction between gas and solid. Thermal conductivity of the electrodes only include the electrode material itself and obtained from Janardhanan.[15]

Electrochemical model

The oxygen anions from reduced oxygen at cathode pass through the electrolyte and react with hydrogen at the anode/electrolyte interface:

$$\frac{1}{2}O_2 + 2e^- \rightarrow O^{2-} \tag{1}$$

$$H_2 + O^{2-} \rightarrow H_2O + 2e^- \tag{2}$$

Thus, the overall chemical reaction is

$$H_2 + \frac{1}{2}O_2 \rightarrow H_2O \tag{3}$$

The Butler-Volmer kinetic equations are generally adopted for expressing the local current density distribution.[16–18]

$$i_a = i_{a,0}\left\{\exp\left(\beta\frac{n_e \cdot F \cdot \eta_{act}}{R_g \cdot T}\right) - \exp\left[-(1-\beta)\frac{n_e \cdot F \cdot \eta_{act}}{R_g \cdot T}\right]\right\} \tag{4a}$$

$$i_c = i_{c,0}\left\{\exp\left(\beta\frac{n_e \cdot F \cdot \eta_{act}}{R_g \cdot T}\right) - \exp\left[-(1-\beta)\frac{n_e \cdot F \cdot \eta_{act}}{R_g \cdot T}\right]\right\} \tag{4b}$$

$$i_{a,0} = \beta_a \cdot \left(\frac{p_{H_2}}{p^{ref}}\right)^{0.25}\left(\frac{p_{H_2O}}{p^{ref}}\right)^{-0.5}\exp\left(-\frac{E_{act,a}}{R \cdot T}\right) \tag{4c}$$

$$i_{c,0} = \beta_c \cdot \frac{\left(p_{O_2}/p^0_{O_2}\right)^{1/4}}{1+\left(p_{O_2}/p^0_{O_2}\right)^{1/2}} \tag{4d}$$

$$p^0_{O_2}(Pa) = 4.9\times10^3\exp\left(-\frac{2\times10^5}{R \cdot T_s}\right) \tag{4e}$$

In Eqs. 4c and 4d, β_a and β_c are the adjustable parameters to fitting the experimental data. The anodic exchange current density can be formulated by Costamagna,[17] β_a is 3.4×10^{10} A/m^2 for a Ni-YSZ anode. The cathodic exchange current density can be formulated by Zhu,[18] where $p^0_{O_2}$ can be found. β_c is 4000 A/m^2 for a LSM-YSZ cathode. The activation loss can be calculated according to the following equation:

$$\eta_{act} = \phi_{rev} - |\phi_{electrode} - \phi_{ele}| \tag{5}$$

where ϕ_{rev} is the reversible potential between the electrode and the electrolyte. ϕ_{rev} can be obtained from Nernst equation. Since the electrochemical active layer is usually very thin compared with the electrode, the current generation is considered to take place only at the electrode/electrolyte interfaces.[2,19]

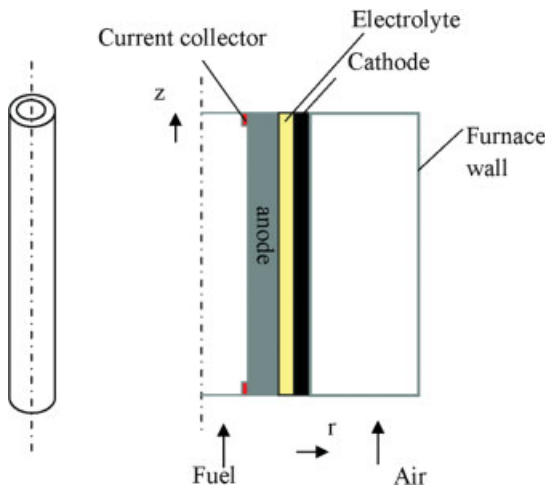

Figure 2. Schematic of a microtubular geometry in 2D.

[Color figure can be viewed in the online issue, which is available at www.interscience.wiley.com.]

In Eqs. 4a and 4b, $i_{a,0}$, $i_{c,0}$ and β are the exchange current density and the transfer coefficient. Since the electrochemical reactions are considered to only occur at the electrode/electrolyte interfaces, electron and ion transport only takes place in the electrode and electrolyte, respectively. Electron and ion charge conservation at the electrode and electrolyte is expressed by Eq. 6.

$$-\nabla(\sigma\cdot\nabla\phi)=0 \tag{6}$$

Momentum and mass transport equations

In this article, properties of pure gases including isobaric molar heat capacity, dynamic viscosity and heat conductivity can be calculated by a function of temperature with fifth order polynomial, respectively as shown in Eqs. 7–9. The coefficients a_n, b_n, and c_n can be found from the Table 2. The heat capacity of mixture gas depends on composition proportion and can be calculated from Eq. 10. Dynamic viscosity and heat conductivity of mixture gas can not been directly calculated from composition proportion. According to Todd,[14] Reichenberg's and Wassiljevas's method for viscosity and conductivity are adopted in this model, respectively.

$$C_P(\mathrm{kJ/kg\cdot K})=\frac{1}{m_i}\sum_{n=0}^{6}a_n\left(\frac{T(K)}{1000}\right)^n \tag{7}$$

$$\mu(Pa\cdot s)=1\times10^7\sum_{n=0}^{6}b_n\left(\frac{T(K)}{1000}\right)^n \tag{8}$$

$$k(\mathrm{W/m\cdot K})=0.01\sum_{n=0}^{6}c_n\left(\frac{T(K)}{1000}\right)^n \tag{9}$$

$$C_p=\sum_{i=1}^{n}x_i\cdot C_{pi}(T) \tag{10}$$

To calculate the velocity distribution in the gas channel, the steady-state incompressible Navier-Stokes equation, Eqs. 11a and 11b are solved numerically:

$$\rho(u\cdot\nabla u)-\mu(\nabla^2u)+\nabla P=0 \tag{11a}$$

$$\nabla u=0 \tag{11b}$$

Brinkman equation is used for the porous media.[2]

$$\nabla P=\mu\cdot\nabla^2u+\frac{\mu}{K}u \tag{12}$$

where K is the permeability of the medium.

The steady-state diffusion and convection equation, Eq. 13 is solved from the velocity distribution to obtain the concentration distribution of reactants and products in the gas channel and the electrodes.

$$\nabla(-D_{ij}\cdot\nabla c_i+c_i\cdot u)=0 \tag{13}$$

Faraday's law is used to evaluate the molar flux at the electrode/electrolyte interfaces:

$$-n\cdot N_{\mathrm{H_2}}=\frac{-i_a}{2F} \tag{14a}$$

Table 2. The Coefficients of Isobaric Molar Heat Capacity, Dynamic Viscosity And Thermal Conductivity

	H_2	H_2O	O_2	N_2
a_0	21.157	37.373	34.85	29.027
a_1	56.036	−41.205	−57.975	4.8987
a_2	−150.55	146.01	203.68	−38.040
a_3	199.29	−217.08	−300.37	105.17
a_4	−136.15	181.54	231.72	−113.56
a_5	46.903	−79.409	−91.821	55.554
a_6	−6.4725	14.015	14.776	−10.350
b_0	15.553	−6.7541	−1.6918	1.2719
b_1	299.78	244.93	889.75	771.45
b_2	−244.34	419.50	−892.79	−809.20
b_3	249.41	−522.38	905.98	832.47
b_4	−167.51	348.12	−598.36	−553.93
b_5	62.966	−126.96	221.64	206.15
b_6	−9.9892	19.591	−34.754	−32.430
c_0	1.5040	2.0103	−0.1857	−0.3216
c_1	62.892	−7.9139	11.118	14.810
c_2	−47.190	35.922	−7.3734	−25.473
c_3	47.763	−41.390	6.7130	38.837
c_4	−31.939	35.993	−4.1797	−32.133
c_5	11.972	−18.974	1.4910	13.493
c_6	−1.8954	4.1531	−0.2278	−2.2741

$$-n\cdot N_{\mathrm{H_2O}}=\frac{i_a}{2F} \tag{14b}$$

$$-n\cdot N_{\mathrm{O_2}}=\frac{-i_c}{4F} \tag{14c}$$

In Eqs. 14a–14c, $n{\cdot}N_i$ denotes species i normal flux along the specified boundary.

Figure 3 depicts a scheme of the different domains together with the governing equations and the boundary conditions at the electrochemical reaction interface.

In Eq. 15, D_{ij} is the mass diffusion coefficient, which are obtained from the reference[14]:

$$D_{ij}=\frac{1.43e^{-7}T^{1.75}}{p\cdot M_{ij}^{1/2}(V_i^{1/3}+V_j^{1/3})^2} \tag{15}$$

$$\text{where } M_{ij}=2(1/m_i+1/m_j)^2 \tag{16}$$

Diffusion in porous electrode is usually described by molecular diffusion or Knudsen diffusion.[19] The overall effective diffusion coefficient is given by the following equation:

$$D_{ij}^{ef}=\frac{\varepsilon}{\tau}\left(\frac{1}{D_{ij}}+\frac{1}{D_K}\right)^{-1} \tag{17}$$

The Knudsen diffusion coefficient D_k can be obtained from Eq. 18:

$$D_K=97r_p\sqrt{T/m_i} \tag{18}$$

Heat generation mechanisms

Most of the heat generated in the SOFC is due to reversible and irreversible processes occurring at the electrode/electrolyte interfaces. Since these processes are surface phenomena in this model, the corresponding heat generation terms are appropriately modeled as surface heat sources. Reversible

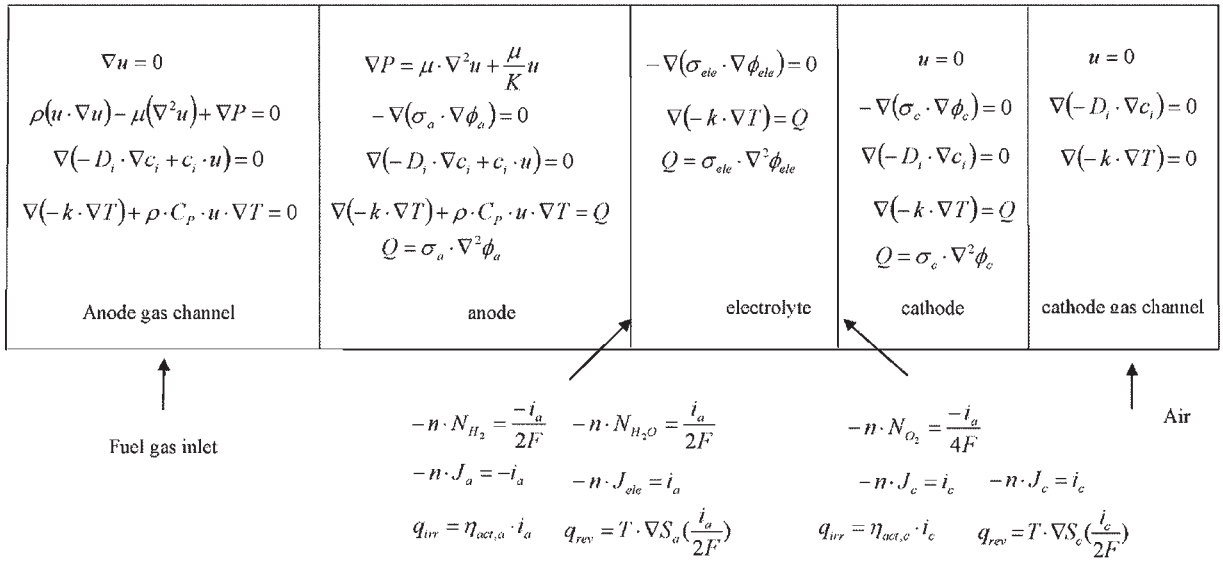

Figure 3. Scheme of all governing equations with the boundary conditions at the electrochemical reaction interface.

heat generation is due to the electrochemical reactions entropy change at the cathode and anode

$$q_{\mathrm{rev},a} = T\cdot\Delta S_a\frac{i_a}{2F} \tag{19a}$$

$$q_{\mathrm{rev},c} = T\cdot\Delta S_c\frac{i_c}{2F} \tag{19b}$$

where i_a and i_c is the local current density, F is the Faraday's constant, and the ΔS_a and ΔS_c denote the molar entropy change of anode and cathode reaction at the local reacting temperature and pressure. The heat is produced at the cathode/electrolyte interface and consumed at the anode/electrolyte interface,[1,20] so Eqs. 1 and 2 are exothermic and slightly endothermic, respectively. Eqs. 19a and 19b cannot be solved directly because the molar entropy change of half-reaction stages are generally unknown. Instead, an experimental value for the entropy change at the cathode is taken from Kanamura.[20] The entropy change at the anode is then calculated from the relation $\Delta S_a = \Delta S_{tot} - \Delta S_c$, where ΔS_{tot} is the overall entropy change associated with Eq. 3. As temperature and partial pressures of i are changed, the molar entropy of i is given by Eq. 20.

$$S_i = S_i^0 + \int_{298}^{T}\frac{C_{P_{i(T)}}}{T_i}dT - R\int_{01325}^{P}\frac{dP}{P_i} \tag{20}$$

The total entropy change can be written by the following equation:

$$\Delta S_{\mathrm{tot}} = S_{\mathrm{H_2O}} - S_{\mathrm{H_2}} - \frac{1}{2}S_{\mathrm{O_2}} \tag{21}$$

Irreversible heat generation at the electrode/electrolyte interfaces is caused by the irreversibilities associated with ion transfer across these interfaces, which are often referred to as the cathodic and anodic overpotentials, η_c and η_a, respectively. Their quantities are most often expressed in units of volts, and accordingly the corresponding heat generation expression:

$$q_{\mathrm{irr},a} = \eta_{\mathrm{act},a}\cdot i_a \tag{22a}$$

$$q_{\mathrm{irr},c} = \eta_{\mathrm{act},c}\cdot i_c \tag{22b}$$

The electrode overpotentials can be estimated from Eqs. 4a and 4b. The third source of heat generation is the ohmic heating in the electrode and electrolyte due to the conduction of electrons and oxygen ions, respectively.

$$Q = \sigma\cdot\nabla^2\phi \tag{23}$$

where σ is the conductivity of the electrode and electrolyte. Although this effect is neglected when simulating most other types of fuel cells, Ohmic heating must be included in tubular SOFC models due to the longer current path compared to other types fuel cells.

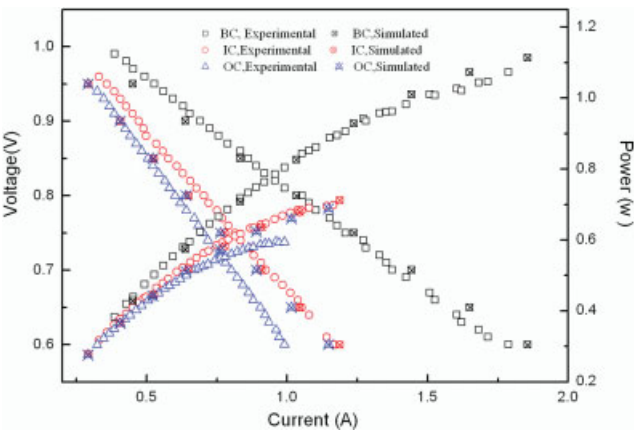

Figure 4. Comparison of simulated and experimental performance data.

[Color figure can be viewed in the online issue, which is available at www.interscience.wiley.com.]

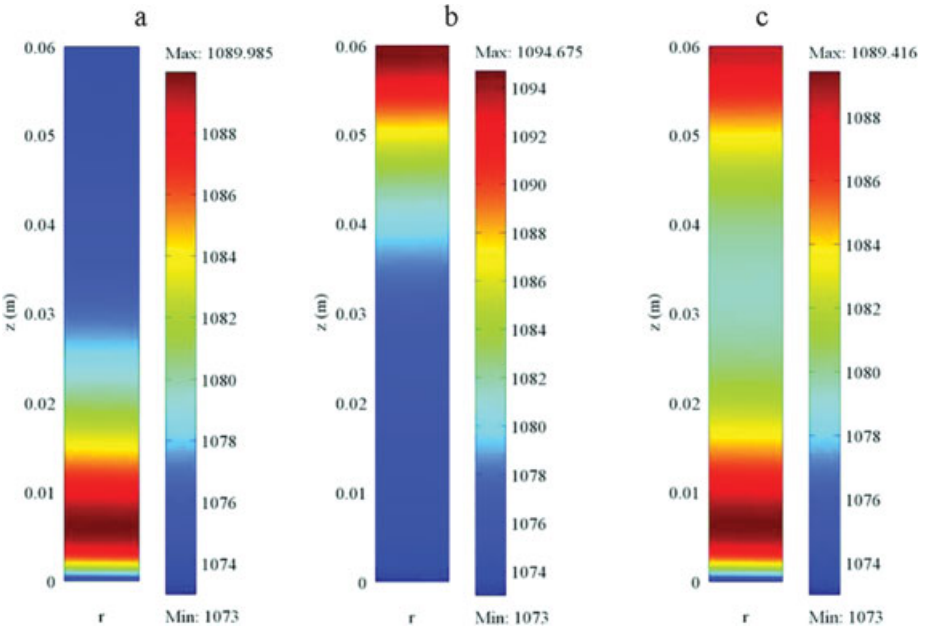

Figure 5. Surface plots of the cell temperature distribution (K) under IC (a), OC (b) and BC (c) modes.

[Color figure can be viewed in the online issue, which is available at www.interscience.wiley.com.]

Heat transfer description

In this model, all three modes of heat transfer are present, including conduction, convection and radiation. Heat generated in the electrodes and electrolyte of the SOFC is transported to the cell exterior predominantly by conduction, and then removed to outside by convection at gas channel and radiation between electrode and gas channel in this model. The temperatures of the inlet fuel and furnace wall are 800°C. The thermal model allows the calculation of the local temperature distribution, which affects the fuel cell performance by the electrochemical reaction rate, the electrode overpotential, the electrical and ionic conductivity, and fluid properties. The temperature profile in all subdomains is obtained through the conductive and convective equation:

$$\nabla(-k \cdot \nabla T) + \rho \cdot C_P \cdot u \cdot \nabla T = Q \tag{24}$$

Convective heat transfer between gas and electrode is described by Newton's law of cooling:

$$q_{\text{conv}} = h_{cv}\left(T_{\text{cell}} - T_{\text{gas}}\right) \tag{25}$$

$$h_{cv} = \frac{Nu \cdot k}{D_h} \tag{26}$$

where h_{cv} is the convective heat transfer or film coefficient. In this model, gas flows in the channels are supposed to a fully developed laminar flow in which the value of *Nu* holds constant at 3.657. Hydraulic diameter is the same to geometric diameter at anode channel:

$$D_{h,a} = D_{a,\text{in}} \tag{27}$$

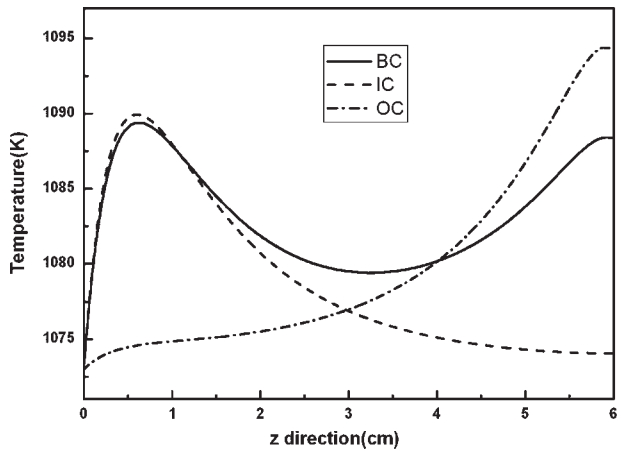

Figure 6. Variation of temperature at the anode/electrolyte interface along z direction.

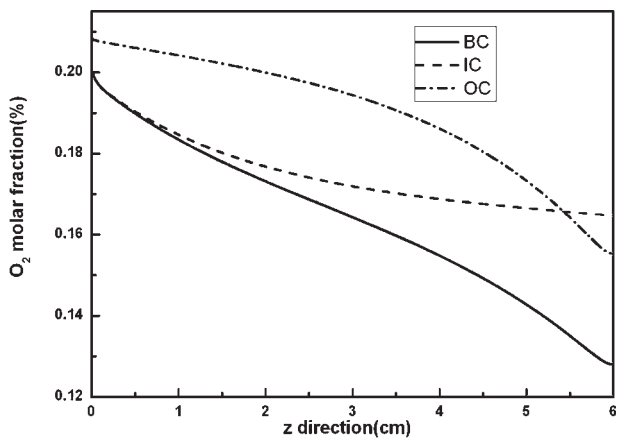

Figure 7. O_2 molar fraction at the cathode/electrolyte interface along z direction.

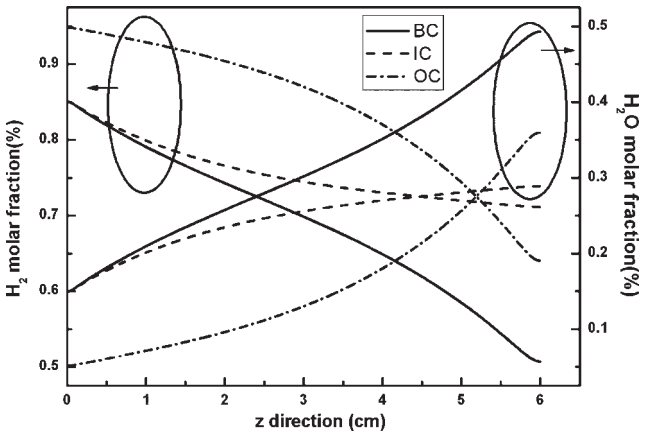

Figure 8. H_2 and H_2O molar fractions at the anode/electrolyte interface along z direction.

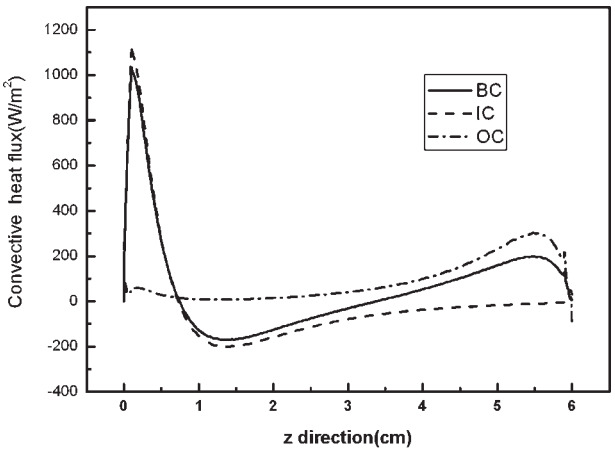

Figure 10. The convective heat flux between anode and fuel gas along z direction under all modes.

Hydraulic diameter is equal to the difference between exterior and interior geometric diameter at cathode channel:

$$D_{h,c} = D_{\text{wall}} - D_{c,\text{out}} \tag{28}$$

Radiative heat transfer between cathode outer surface and furnace wall are expressed as Eq. 28:

$$q_{\text{rad}} = \sigma_0 \cdot \varepsilon_{\text{rad}} \left(T_c^4 - T_{\text{wall}}^4\right) \tag{29}$$

Numerical solution

The governing equations are solved with the commercial software, COMSOL MULTIPHSICS®. In this article, we choose to create a free mesh consisting of triangular elements for a 2D geometry in COMSOL Multiphysics. Mesh consists of 58,521 elements. With the cell voltage changed, the cell performances were obtained from the model. The outputs from the model are the distributions of temperature, current density and species concentrations.

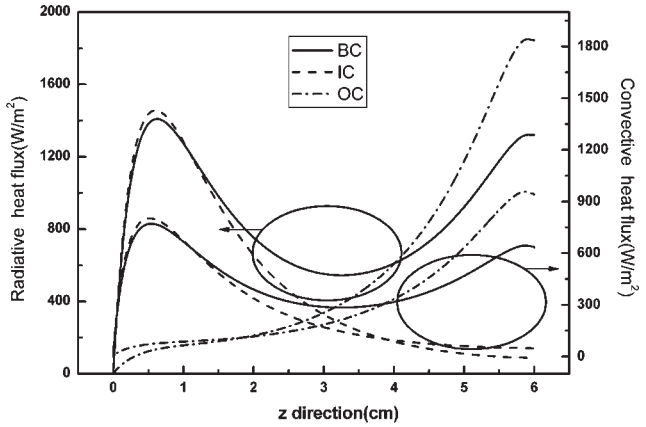

Figure 9. The convective heat flux and radiative heat flux between cathode and environment along z direction under all modes.

Results and Discussion

Model validation

In the article, we focus our attention on the performance of humidified (3% H2O) hydrogen entering a micro tubular SOFC. With the cell voltage changed, the cell performances obtained from the model are compared with the experimental performance data as shown in Figure 4. The simulation results show that the calculated polarization curves agree very well with the experimental data in most cases. We noticed that the experiment data are lower than the calculated ones at OC mode. This phenomenon is thought to be caused by omitting the resistance at longer external circuit at OC mode than the other modes in the experiment. These demonstrate that the present model is accurate enough for use in studying the cell behavior of a tubular SOFC operating with humidified hydrogen.

Temperature and species distribution

Figure 5 shows the surface plots of the cell temperature distribution under IC (a), OC (b) and BC (c) modes. Temperature gradually increases from inlet to outlet. The temperature difference in r direction is smaller than that in z direction, and the temperature variation under IC and BC modes is larger at the inlet than outlet. Figure 6 shows the variation of temperature at the anode/electrolyte interface along z direction. The temperature variation trend along z direction is more clearly depicted. Temperature rapidly increases at inlet for IC and BC modes, and then decreases, yet, it increases at outlet for BC mode. Temperature always increases for OC mode.

Figure 7 shows the changes of O_2 molar fraction at the cathode/electrolyte interface along z direction. Figure 8 shows the variation of H_2 and H_2O molar fraction at the anode/electrolyte interface along z direction. H_2 and O_2 molar fraction decreases along the gas-flow direction under all modes, and H_2O molar fraction increases. The results are similar to those reported by Cui.[2] At inlet, the curves of

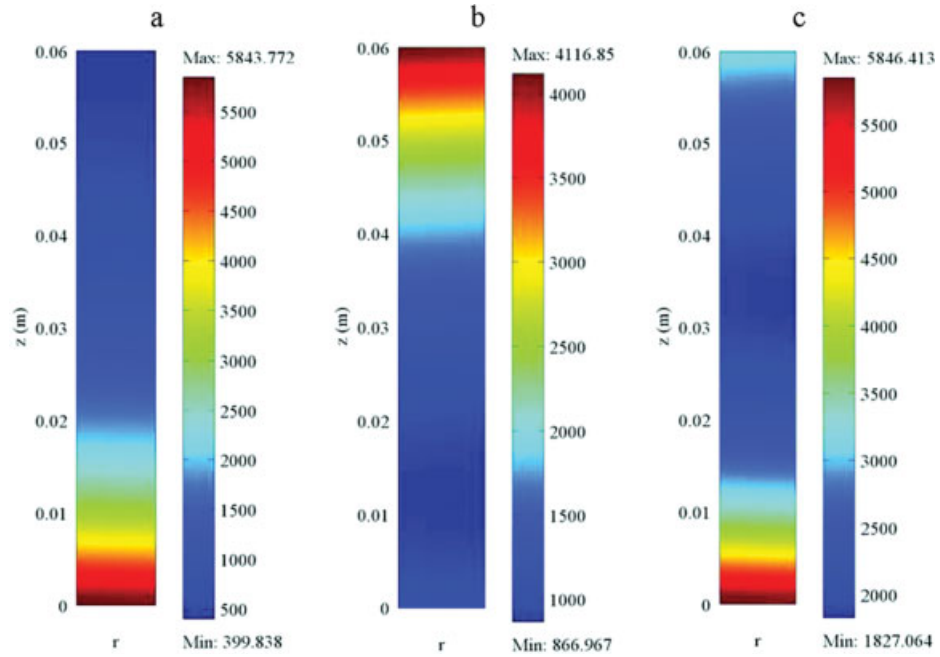

Figure 11. Surface plots of current density distribution (A/m^2) at electrolyte under IC (a), OC (b) and BC (c) modes.

[Color figure can be viewed in the online issue, which is available at www.interscience.wiley.com.]

species change are similar for IC and BC mode; at outlet, those for OC and BC mode have the similar gradient.

Heat transfer phenomena and current density distribution

Figure 9 shows the convective heat flux and radiative heat flux between cathode and environment along z direction under all modes. Cathode exchanges heat with environment by the two heat transfer modes in this model. The convective heat flux is about half as much as radiative heat flux between cathode and environment. Figure 10 shows the convective heat flux between anode and fuel gas along z direction under all modes. From the Eqs. 25 and 26, it can be found that the temperature difference between electrode and gas is the dominating factor for the convective heat flux. This indicates that the temperature difference nearby inlet under IC and BC modes is higher than the other places. From Figures 9 and 10, it is found that the heat transfer at cathode is the dominating transport mode in this model.

The resistive heating at electrolyte is the main heat source in this model, and the current density distribution decides the resistive heating variation. Figure 11 shows the surface plots of current density distribution at electrolyte under all modes. The current density under BC mode firstly decreases and reaches a minimum in the middle part, and then increases toward the outlet. The maximum of current density under the IC mode appears at inlet, and the minimum arises at outlet. The current density at inlet under the IC and BC modes are both close to 5850 A/m^2. The current density at outlet under IC mode is 400 A/m^2, which is smallest among all modes. For OC mode, the current density difference between the maximum and minimum is only 3249 A/m^2, which is smallest among all modes. The curves in Figure 12 represent the current density at the left boundary of Figure 11, which shows the current density variation at the anode/electrolyte interface along z direction. Figure 12 represents the current density variation trend at electrolyte and shows more intuitionistic results. Figure 13 shows surface plots of resistive heating distribution at electrolyte under all modes. The resistive heating distribution is similar to current density distribution. For IC and BC mode, the resistive heating maximum is both about 1.497×10^7 W/m^3. The difference of resistive heating between the maximum and the minimum at OC mode is the smallest among all modes. So, the OC mode is the optimal mode for long-life cell operation among the all modes considering more uniform heat flux, temperature and current density distribution.

The resistive heating at anode is relatively less than that at electrolyte because of higher anodic conductivity. But, the

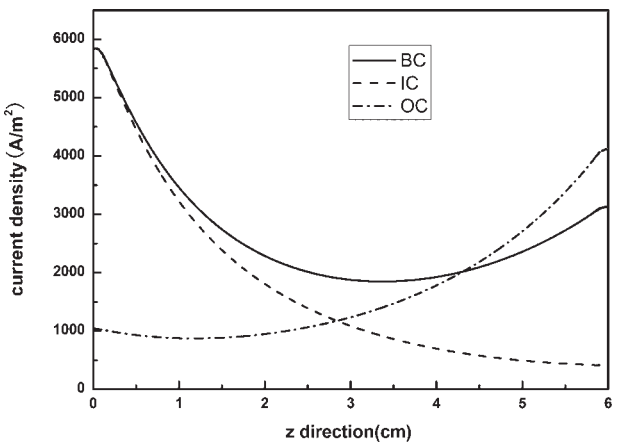

Figure 12. Distribution of current density at the anode/electrolyte interface along z direction.

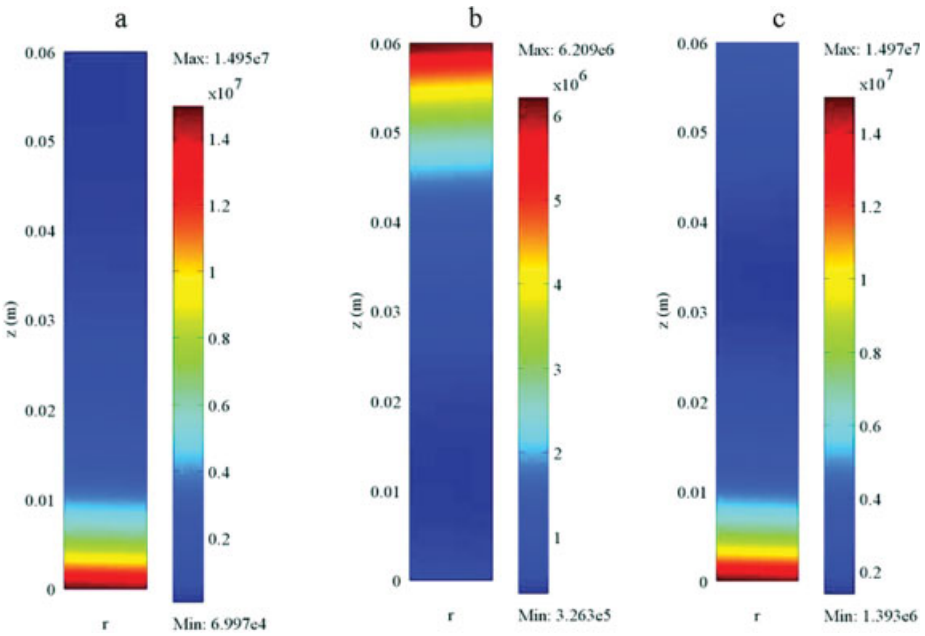

Figure 13. Surface plots of resistive heating distribution (W/m^3) at electrolyte under IC (a), OC (b) and BC (c) modes.

[Color figure can be viewed in the online issue, which is available at www.interscience.wiley.com.]

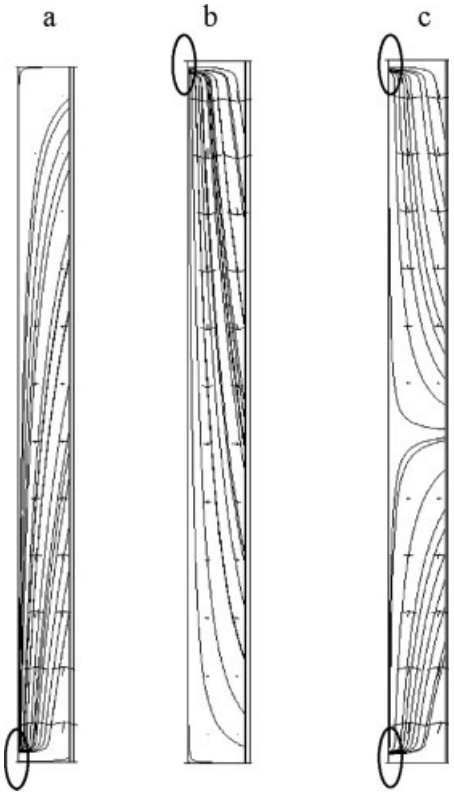

Figure 14. The streamline and arrow plots of the anodic current density under IC (a), OC (b) and BC (c) modes.

current density distribution as well as resistive heating variation at anode are not very uniform. Figure 14 shows streamline and arrow plots of the anodic current density under all modes. In Figure 14, the streamlines and arrows express current-flow directions, and the arrow lengths are proportional to current density. The current flow in anode is evidently not parallel to the anode/electrolyte interfaces, and a majority of current flow is from a point into anode. To understand the phenomena, the height is added to express the current density distribution at anode. Figure 15 shows a 3D contour plot of

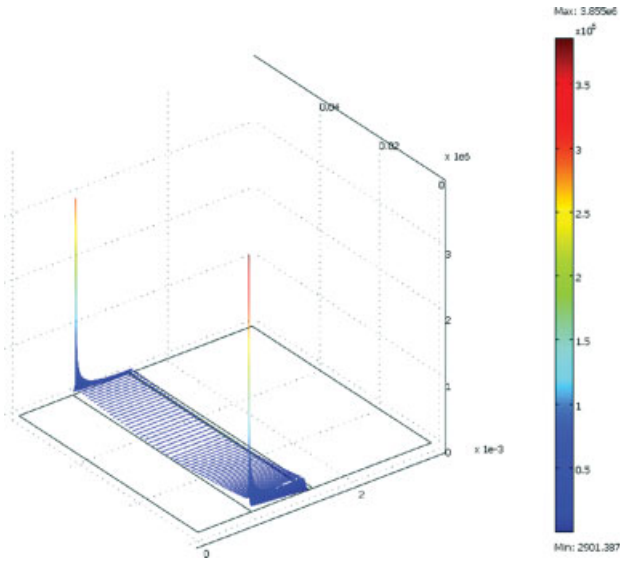

Figure 15. 3D contour plot of the anodic current density (A/m^2) under BC mode.

[Color figure can be viewed in the online issue, which is available at www.interscience.wiley.com.]

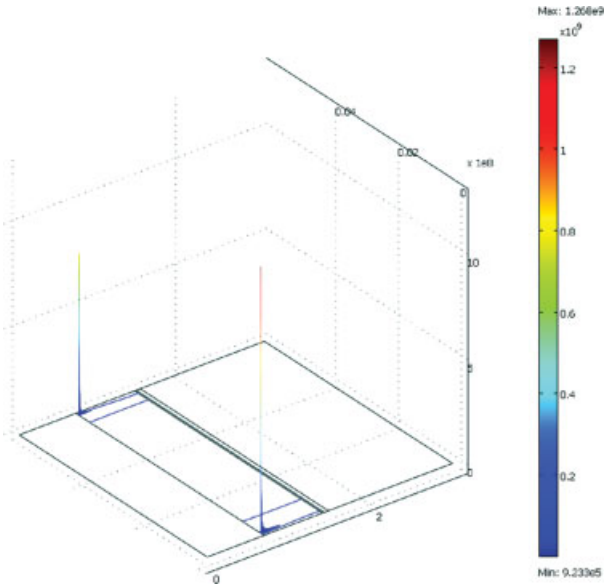

Figure 16. 3D contour plot of the anodic resistive heating (W/m^3) under BC mode.

[Color figure can be viewed in the online issue, which is available at www.interscience.wiley.com.]

the anodic current density under BC mode. From Figure 15, the highest current density point is evidently close to current collector and just like a needle. The current coming into anode is mainly from a point which locates in front of current collector. The phenomena show that the most current-flow goes into anode from a very small area because the current collectors are at the ends. This result indicates that the current collector area has less effect to collect current. Figure 16 shows 3D contour plot of the anodic resistive heating under BC mode. The resistive heating distribution is also similar to current density distribution, and a peak can be found around the current collector. Though a very high point can be also found from the resistive heating distribution at anode, no hot spots appear at anode because of the more rapidly heat transfer rate.

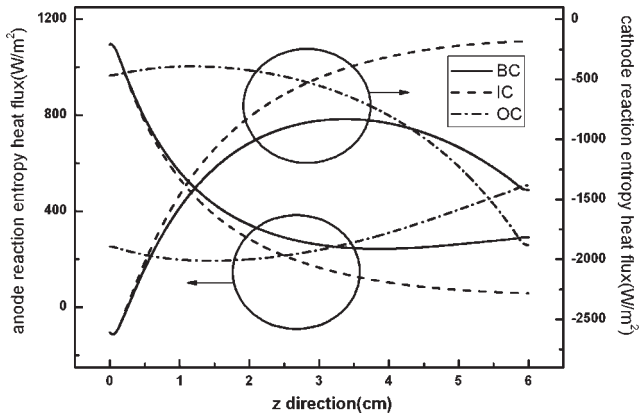

Figure 18. Anode and cathode reaction entropy heat flux at electrode/electrolyte interface along z direction.

The heat generated by the electrochemical reaction in this model is supposed to occur at the electrode/electrolyte interfaces. Figure 17 shows that the overall reaction entropy change decreases along the electrode/electrolyte interface. From Eqs. 20 and 21, it can be found that reaction entropy change decreases when reactant fraction decreases. Because H_2 and O_2 fractions decrease and H_2O fraction increases along gas-flow direction from Figures 7 and 8, the overall reaction entropy change decreases.

The reaction entropy heat is calculated by Eqs. 19a and 19b, in which entropy change and current density are the dominant factors. Figure 18 shows anode and cathode reaction entropy heat flux at electrode/electrolyte interface along z direction. The heat due to reaction entropy change is consumed at the anode/electrolyte interface and produced at the cathode/electrolyte interface. The absolute value of the heat due to reaction entropy change at cathode/electrolyte interface is about twice as much as that at anode/electrolyte interface. Figure 19 shows overall heat flux at electrode/electrolyte interfaces along z direction. The overall electrochemical reaction heat is consumed at the anode/electrolyte interface

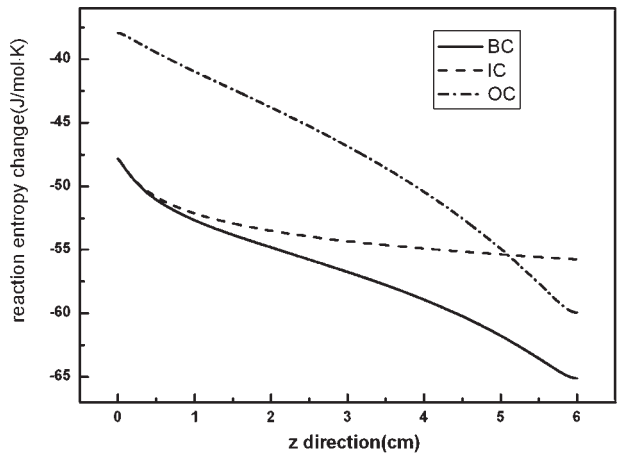

Figure 17. Overall reaction entropy change at the electrode/electrolyte interface along z direction.

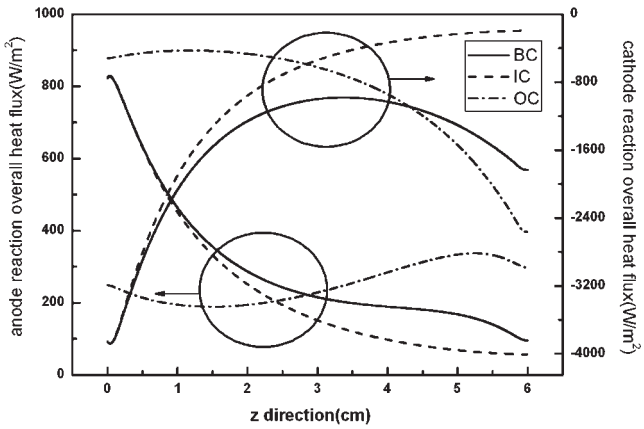

Figure 19. Overall heat flux at electrode/electrolyte interfaces along z direction.

and produced at the cathode/electrolyte interface. The heat produced at cathode/electrolyte interface is about five times as much as that consumed at anode/electrolyte interface.

Conclusions

In this article, a 2D numerical model considering momentum, heat/species transport and electrochemical phenomenon, has been proposed and proved to be a valuable and high efficient model for the analysis of microtubular SOFC. The variations of species concentrations and temperature distribution in 2D have been obtained. The validation results showed that the model agrees well with the experimental data. The overall electrochemical reaction heat is produced at cathode/electrolyte interface, and a small portion of the heat is consumed at anode/electrolyte interface in this model. The heat produced at cathode/electrolyte interface is about five times as much as that consumed at anode/electrolyte interface. The overwhelming part of the heat transfer between cell and outside occurs at cathode external surface in this model, including convective and radiative modes. The temperature distributions under IC and BC modes show that the nonuniform temperature variation is more serious at inlet than at outlet. The simulated current path inside the anode-supported microtubular SOFC clearly reflect the current flow in a tubular cell. The current going into anode is mainly from a point which locates in front of current collector. The result indicate that the current collector area has less effect on current collecting. A very high resistive heating point is found at anode, but it is not a hot spot because of the rapid heat transfer rate.

Acknowledgments

The authors gratefully acknowledge financial supports from the Ministry of Science and Technology of China (No. 2004CB719506, 2005CB221404, and 2006AA05Z147) and Natural Science Foundation of China (No. 20676132).

Notation

c_i = the i species concentration, mol/m^3
C_p = specific heat capacity, kJ/kg K
D_h = hydraulic diameter, m
D_{ij} = molecular diffusion coefficient, m^2/s
E_0 = standard potential, V
$E_{act,a}$ = activation energy of anode, J/mol
F = Faraday's constant, 96,485C/mol
h_{cv} = convective thermal coefficient, W/m^2 K
k = thermal conductivity, W/m K
K = permeability, m^2
m_i = molecular weight of the i species, kg/kmol
n_e = electron transferred per reacting
Nu = Nusselt number
i = current density, A/m^2
i_0 = exchange current density, A/m^2
P = pressure, Pa
P^{ref} = referance pressure, 10^5Pa
q = heat source, W/m^2
Q = volumetric heating rate, W/m^3
R_p = porous radius, m
R_g = gas constant, 8.314 J/mol·K
ΔS_a = the molar entropy change of anode reaction, J/mol·K
ΔS_c = the molar entropy change of cathode reaction, J/mol·K
T = temperature, K
u = velocity, m/s
V_i = Fuller diffusion volume of the i species

Greek letters

β = transfer coefficient
β_a = Pre-exponential coefficient for anode in Eq. 4c, A/m^2
β_c = Pre-exponential coefficient for cathode in Eq. 4d, A/m^2
ε = porosity
ε_{rad} = thermal radiative emissivity
η = overpotential, V
μ = dynamic viscosity, Pa·s
ρ = density, kg/m^3
σ = conductivity, S/m
σ_0 = Stefan-Boltzmann constant, 5.67×10^{-8} W/m^2 K^4
τ = tortuosity factor
Φ = potential, V

Subscripts and superscripts

a = Anode
act = activation
c = cathode
conv = convection
diff = diffusion
ef = effective
ele = electrolyte
irr = irreversible
K = Knudsen diffusion
m = ordinary diffusion
rad = radiation
rev = reversible
tot = total

Literature Cited

1. Singhal SC, Kendall K. *High Temperature Solid Oxide Fuel Cells: Fundamentals, Design and Applications*. Kidlington Oxford: Elsevier, 2003.
2. Cui DA, Liu L, Dong YL, Cheng MJ. Comparison of different current collecting modes of anode supported micro-tubular SOFC through mathematical modeling. *J Power Sources*. 2007;174:246–254.
3. Sanchez D, Chacartegui R, Munoz A, Sanchez T. Thermal and electrochemical model of internal reforming solid oxide fuel cells with tubular geometry. *J Power Sources*. 2006;160:1074–1087.
4. Bove R, Sammes NM. The effect of current collectors configuration on the performance of a tubular SOFC. In: Proceedings of the ninth international symposium on solid oxide fuel cells (SOFC IX), May 15–20, Quebec City, Canada, 2005.
5. Achenbach E. Three-dimensional and time-dependent simulation of a planar solid oxide fuel cell stack. *J Power Sources*. 1994;49:333–348.
6. Iwata M, Hikosaka T, Moriya M, Iwanari T, Ito K, Onda K, Esaki Y, Sakai Y, Nagata S. Performance analysis of planar-type unit SOFC considering current and temperature distributions. *Solid State Ionics*. 2000;132:297–308.
7. Yakabe H, Ogiwra T, Hishinuma M, Yasuda I. 3-D model calculation for planar SOFC. *J Power Sources*. 2001;102:144–154.
8. Yakabe H, Sakurai T. 3D simulation on the current path in planar SOFCs. *Solid State Ionics*. 2004;174:295–302.
9. Lockett M, Simmons MJH, Kendall K. CFD to predict temperature profile for scale up of micro-tubular SOFC stacks. *J Power Sources*. 2004;131:243–246.
10. Du YH, Sammes NM. Fabrication and properties of anode-supported tubular solid oxide fuel cells. *J Power Sources*. 2004;136:66–71.
11. Pusz J, Smirnova A, Mohammadi A, Sammes NM. Fracture strength of micro-tubular solid oxide fuel cell anode in redox cycling experiments. *J Power Sources*. 2007;163:900–906.
12. Sammes NM, Du YH, Bove R. Design and fabrication of a 100 W anode supported micro-tubular SOFC stack. *J Power Sources*. 2005;145:428–434.

13. Suzuki T, Yamaguchi T, Fujishiro Y, Awano M. Current collecting efficiency of micro tubular SOFCs. *J Power Sources*. 2006;163:737–742.
14. Todd B, Young JB. Thermodynamic and transport properties of gases for use in solid oxide fuel cell modelling. *J Power Sources*. 2002;110:186–200.
15. Janardhanan VM, Deutschmann O. Numerical study of mass and heat transport in solid-oxide fuel cells running on humidified methane. *Chem Eng Sci*. 2007;62:5473–5486.
16. Chan SH, Khor KA, Xia ZT. A complete polarization model of a solid oxide fuel cell and its sensitivity to the change of cell component thickness. *J Power Sources*. 2001;93:130–140.
17. Costamagna P, Honegger K. Modeling of solid oxide heat exchanger integrated stacks and simulation at high fuel utilization. *J Electrochem Soc*. 1998;145:3995–4007.
18. Zhu H, Kee RJ, Janardhanan VM, Deutschmann O, Goodwin DG. Modeling elementary heterogeneous chemistry and electrochemistry in solid-oxide fuel cells. *J Electrochem Soc*. 2005;152: A2427.
19. Bove R, Ubertini S. Modeling solid oxide fuel cell operation: approaches, techniques and results. *J Power Sources*. 2005;159:543–559.
20. Kanamura K, Yoshioka S, Takehara Z. Dependence of entropy change of single electrodes on partial pressure in solid oxide fuel cells. *J Electrochem Soc*. 1991;138:2165–2167.

Manuscript received Mar. 20, 2008, and revision received Sept. 7, 2008.